Solid Freeform Fabrication 2024: Proceedings of the 35th Annual International Solid Freeform Fabrication Symposium – An Additive Manufacturing Conference
Reviewed Paper

DEVELOPMENT OF A GEOMETRICALLY BASED METHODOLOGY FOR LOCAL PROCESS CONTROL IN POWDER BED FUSION

Holger Merschroth[1], Julius van der Kuip[1], Jana Harbig[1], Michael Kniepkamp[1]

[1] Institute of Production Management, Technology and Machine Tools (PTW), Technische Universität Darmstadt, Darmstadt, Germany

Abstract

Laser powder bed fusion is a widely used additive manufacturing process, which is dependent on various influences. Layer-wise melting of powder generates successive heating and cooling, which affects the local microstructure of the manufactured part. Especially geometry-dependent heat distribution leads to inhomogeneous local solidification and microstructure. Therefore, control strategies are required which locally adapt the process parameter depending on the part geometry and building process. In this paper a voxel-based control strategy for the laser power is designed. A voxel size of 100 µm considers the local heat distribution of each point's vicinity and adjusts the parameter voxel-wise. In addition, a machine-independent methodology is developed to execute the voxel-based parameters in vectors for the laser powder bed fusion process. Furthermore, the limits of the laser power adaption are identified experimentally. The presented results demonstrate an improved part geometry, surface roughness and a homogenization of the material properties.

1. Introduction

Additive manufacturing processes have been increasingly used in industrial manufacturing in recent years. An increase in global sales of additively manufactured products and services was reported by almost 20% from 2022 to 2023 [1]. Layer-by-layer production makes it possible to manufacture complex geometries such as fine structures integrated into closed cavities or cooling channels into walls [2,3,4]. However, the cost and time efficiency for single part production or small series is much higher compared to conventional processes [5]. The desired component can be manufactured direct from the computer-aided design (CAD) model without the need for additional auxiliary tools.

However, manufacturing parts with increasing complexity requires the quality of the manufacturing process to be constantly improved. For example, the dimensional accuracy of additively manufactured channel structures is dependent on their position and orientation within the build space. Horizontal bores and channels tend to exhibit sagging on the upper side [6], which cannot be corrected through subsequent machining in the case of twisted channel structures. In addition, complex quality assurance is often necessary for high-risk components [7]. One way to increase the process quality of additive manufacturing processes is to adjust the process parameters locally within a component. Due to the high geometric complexity of the manufactured components, the process conditions within a component are not uniform. For instance, as the height of the component increases, the heat of the powder to be melted can also increase [8]. By adjusting the process parameters, the homogeneity of the microstructure can be increased. Open and closed

loop controls are investigated to compensate for process inhomogeneities and to enhance dimensional accuracy and surface quality. A common open control loop approach is the upskin and downskin exposure method which involves multiple irradiations and energy input reduction in areas which are in contact with the powder bed [9,10,11]. An example for a closed-loop feedback control was presented by Kavas et al., which enables the in-layer temperature stabilization [12].

In this work an open control loop is developed, which considers the heat distribution inside an additive manufactured part of each point's vicinity. The Powder Bed Fusion with laser beam and metallic powder (PBF-LB/M) process uses a laser beam to melt metallic powder at the desired areas inside each layer to generate the final product. The locally varying energy dissipation causes locally different boundary conditions for the powder melting process which is one main reason for part and surface inhomogeneities. Adjusting the laser power accordingly enables a more stable and homogeneous process and product. Previous works studied the thermal history of parts using neural networks and showed improved mechanical properties [13]. To avoid time and cost consuming data generation and training of a neural networks in this work a geometrically based control approach is developed which generates a voxel-based laser power parameter set. Additionally, a translation of voxel-based to vector-based parameters will be introduced to enable the processing of those parameters.

2. Methodology development

The main influences on the formation of a melt pool and its solidification process are the energy introduced by the laser beam, the heat radiation to the environment and the heat conduction in the building platform, component and powder bed. Energy losses by thermal radiation can be neglected due to the small radiating surface area compared to the volume which contributes to the heat conduction. To account for the described energy balance of the process, a voxel-based parameter set is generated, allowing for locally variable laser power values. These voxel-based parameters (B.2) are generated during process preparation after CAD data preparation (A) and parallel to the scan vectors for the exposure strategy (B.1), which is depicted in Figure 1. Therefore, the position, direction and sequence of the individual scan vectors cannot be considered during analysis, as these are only created according to a fixed pattern at a later point in the data processing chain. The machine, the used material and the process boundary conditions can be assumed to be constant for the power adjustment module presented in this work. Dividing the component into multiple voxels generates a large number of elements (e.g. 320,000,000 for a cuboid with an edge length of 40 mm) which is why the underlying calculation for each element must be kept simple and parallelizable. This is why the developed approach takes only the geometric boundary conditions into account, which have an influence on the melting process.

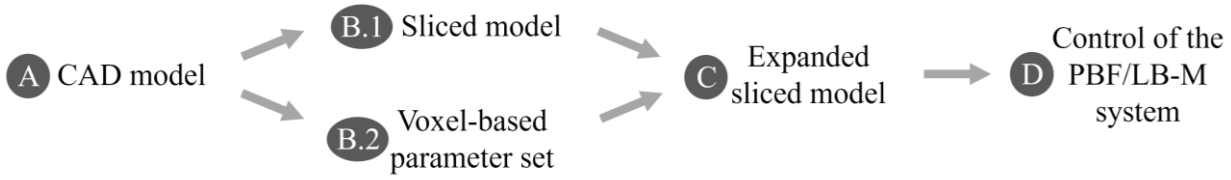

Figure 1: Expanded process preparation and methodological approach

Two cases must be considered while analyzing the heat distribution during the powder exposure. The first case is geometrically stationary and considers the powder being exposed in the component core. The process energy is mainly transferred into the already produced component by heat conduction (Figure 2, left side). The area around the melt pool which heats up during the exposure of the powder is called heat-affected zone. The second case is unsteady due to the heat-affected zone being partly filled with powder (Figure 2, right side). A significant difference in the temperature-dependent thermal conductivities between solid material ($\lambda_s(T)$) and powder ($\lambda_p(T)$) is present because the gas between the powder particles can be considered as an isolator [14]. In the transient case, heat build-up can occur, resulting in an enlargement of the melt pool and thus in unwanted melting of additional material [15,16,17].

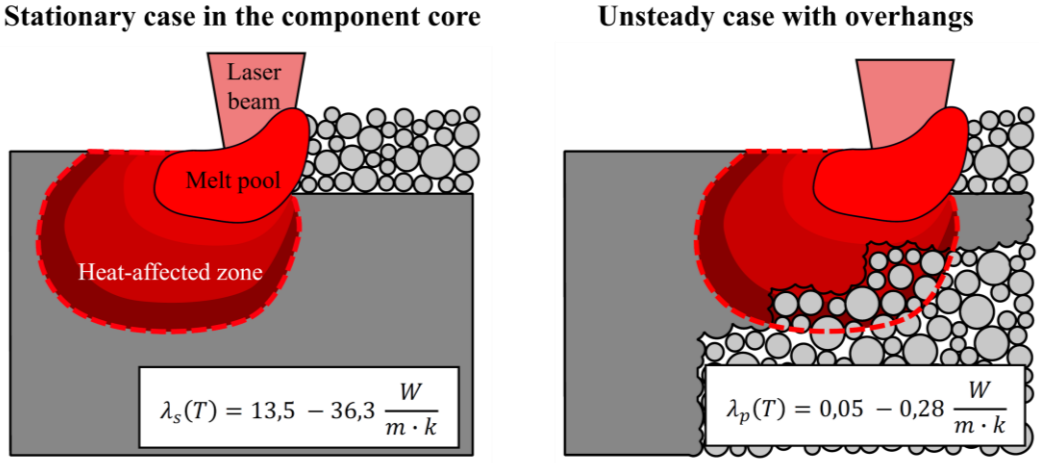

Figure 2: Heat-affected zone in geometrically stationary (left) and unsteady (right) case [14]

In this work, the developed approach sets the volume of solid material in the heat-affected zone in relation to the volume of the powder material. The derived factor will be used to adapt the laser power inside the respective voxel, which aims at a stabilization of the melt pool in critical component areas. To ensure a machine-, material- and parameter-independent approach, the size and shape of the analysis space should be freely definable. This also enables the controllability to which extent geometric aspect are considered. In Figure 3 a 2D simplification of the procedure is illustrated, in which the relation of solid and powder material is analyzed. The voxel grid outlines each defined voxel of the component. Some voxels consist of powder material, whilst others are solid. The active voxel refers to the voxel, which is analyzed during this step. The analysis area describes the area around the active voxel, which is considered as the heat-affected zone and therefore contributes to the heat distribution. The volume of solid material V_1 and the volume of powder material V_2 are calculated using binary 3D matrices which greatly reduces the required computational effort and the amount of memory. The adjusted laser power $P_{\mathrm{l,a}}$ of the current active voxel is calculated using Equation 1 [14].

$$P_{\mathrm{l,a}} = P_{\mathrm{l,min}} + \left(P_{\mathrm{l,q}} - P_{\mathrm{l,min}}\right)\left(\frac{V_1}{V_1 + V_2}\right) \qquad \text{(Eq. 1)}$$

$P_{\mathrm{l,q}}$ represents the laser power of the parameter set already qualified for the geometrically stationary case, which is often referred to as standard parameter. The factor $P_{\mathrm{l,min}}$ ensures that the

calculation does not fall below a definable minimum laser power. This is necessary, as insufficient laser power may prevent the powder from melting. The difference between $P_{l,q}$ and $P_{l,min}$ therefore represents the range in which the laser power can be varied. The calculation is performed for each voxel of the component and the results are stored in a 3D matrix. Since the calculation of a voxel has no influence on the calculation of the adjacent voxels, the calculation of the component analysis can be parallelized and can be greatly accelerated by using multi-core or graphics processors.

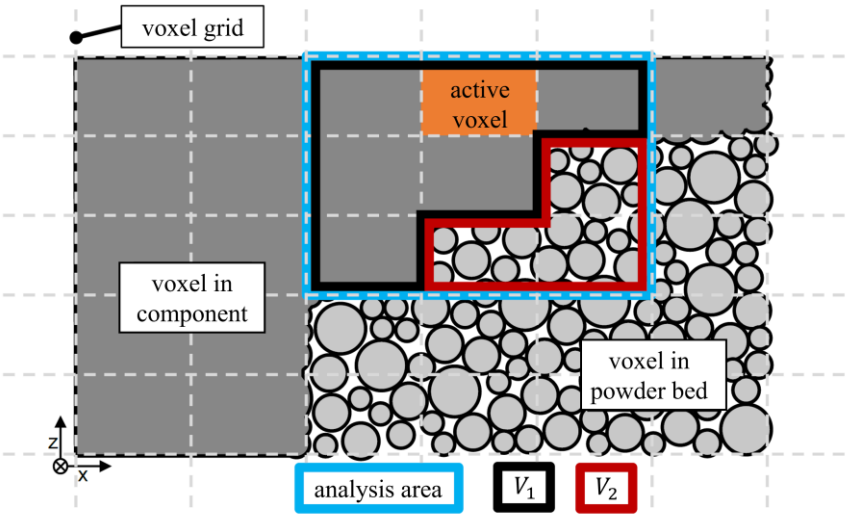

Figure 3: Analysis approach for adapting the laser power to the local geometry conditions [14]

After the creation of the 3D matrix (B.2), containing the adjusted laser power parameters, and the creation of the sliced model (B.1), the next necessary step for processing is the formation of an expanded sliced model (C) (Figure 1). The transformation of those voxel-based parameters into vector-based parameters is visualized in Figure 4. On the left side, the voxel matrix is depicted, with different colors representing varying parameter values. In the middle of Figure 4 all individual vectors of the sliced model are illustrated. The height of a voxel corresponds to the layer height of the sliced model, which is why the number of layers of the sliced model is similar to the number of voxels in vertical direction. To enable a machine processible parameter set the voxel-based parameters have to be transformed to vector-based parameters, which can be integrated to the already sliced model (Figure 4, right side).

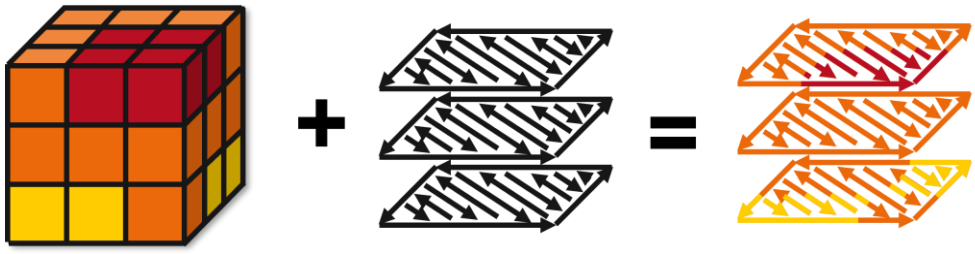

Figure 4: Transformation of voxel-based parameters (left) to vector-based parameters (right).

Therefore, this transformation is performed after the voxel model is generated and the CAD model is sliced. Each vector of the sliced model is geometrically compared to the voxel matrix and parameters are extracted. In Figure 5 the process of a single vector profile generation is displayed. At first, the vector will be geometrically placed inside the corresponding layer of the voxel matrix.

Since the vector is one-dimensional, it will be expanded with the laser beam diameter to a two-dimensional area, which can be seen on the left side of Figure 5 with the gray area and dashed outline. The orientation of the scan vector is independent of the voxel orientation, so each vector must be examined individually. The geometrically independence occurs because the voxels maintain a consistent orientation throughout the entire component, while the scan vectors can rotate within each plane based on the scan strategy.

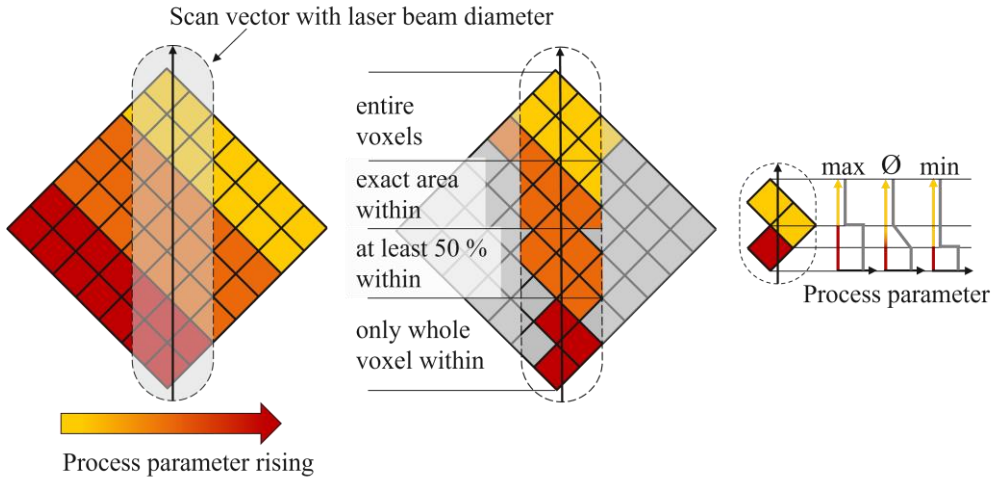

Figure 5: Process of a single vector profile generation

After expanding each vector to an area, this long vector area will be discretized, so several small segments are present inside one vector. This is necessary to generate a parameter profile inside each vector. The discretization step size, which is similar to the minimum vector length, for a parameter change results from the hardware limits of the system. The minimum vector length l_{min} is calculated using Equation 2 based on the specified output period T_{step} of the used control card and the maximum speed v_{laser} used in the experiment.

$$l_{\mathrm{min}} = v_{\mathrm{laser}} \cdot t_{\mathrm{step}} \cdot S \qquad \text{(Eq. 2)}$$

A safety factor S accounts for the potential reduction in the theoretically possible vector length caused by high data transfer rates and interference during transmission. Each of those segments is then analyzed individually to generate a parameter value. The center of Figure 5 illustrates several variants that define the voxels to be considered for the vector-based parameters for one vector segment. These multiple variants enable the emphasis of different parameter distributions. In this work all voxels inside the vector segment are considered, which is referred to in Figure 5 as “exact area within”. Additionally, if the voxel is only partly inside the vector segment, it will also only be weighted proportionally. The selected voxels are then aggregated into a single parameter value, which is assigned to the vector segment. The choice between the mean value of the parameters, the minimum, and maximum values of the parameters within this vector element can be made. In this work the mean value is calculated. The difference between the three methods of aggregation is illustrated on the right side of Figure 5. Each vector segment of each vector inside each layer must be analyzed to generate a complete transfer of a voxel-based to vector-based parameter set. Since each vector segment has no influence on the calculation of the

adjacent segment, this process also can be parallelized and greatly accelerated by using multi-core or graphics processors.

3. Experiments

To validate the developed process control, it is first verified whether the laser power can be adjusted accordingly, which is a crucial step to enable the creation of the expanded sliced model (Figure 1, C). Additionally, it is analyzed whether critical component areas can be identified with the module (Figure 1, B.2). The aim of the final validation is to check whether the component quality can be increased with the usage of the introduced methods.

To verify sufficient adaptability of the laser power for the creation of the expanded sliced model (Figure 1, C) the PBF-LB/M system Aconity MIDI from the manufacturer Aconity3D GmbH is used. This system is characterized by a building chamber with a diameter of up to 170 mm and a height of up to 180 mm as well as a process monitoring system consisting of two on-axis pyrometers and an on-axis high-speed camera. In total, both pyrometers cover a wavelength range from 1450 nm to 1700 nm and 2000 nm to 2200 nm at a frequency of 100 kHz. The output of both pyrometers corresponds to the measured intensity of the melt pool radiation in the form of a voltage signal, whereby the output ranges from 800 mV to 4000 mV. A single-mode fiber laser with the designation CFL-500-SM from nLight is used as the laser source. The maximum power of the laser is 500 W, with a maximum rise and fall time of the laser of 5 µs. A SP-ICE-3 control card from RAYLASE GmbH is used to control all components of the PBF-LB/M system. With an output period of 10 µs, individual components can be controlled at a frequency of 100 kHz. The test chamber is flooded with argon during the test. In addition, an argon protective gas flow ensures the removal of fumes that form when the material melts.

Sufficient adaptability of the laser power is ensured if the transition from the lowest to the highest power value can be achieved within the shortest processing time. Therefore, single line tests are performed wherein the laser power is linear increased and decreased from lowest to highest power value. The test is conducted on an AISI 316L substrate plate without a powder bed to analyze the machine behavior independently of powder melting dynamics. Apart from the laser power, all additional process parameters are sourced from the standard parameter set provided by the manufacturer Aconity GmbH. Figure 6 shows the experimental setup to verify the laser power adjustability. Each vector includes a linear power profile from 0 W to 450 W or from 450 W to 0 W, while the length of the vector decreases which is consequently leading to an increased or decreased slope of the power adjustment. Each vector is performed three times to assure statistical validity. Table 1 contains the dimensions of all vectors from left to right with the constant gap length between all vectors.

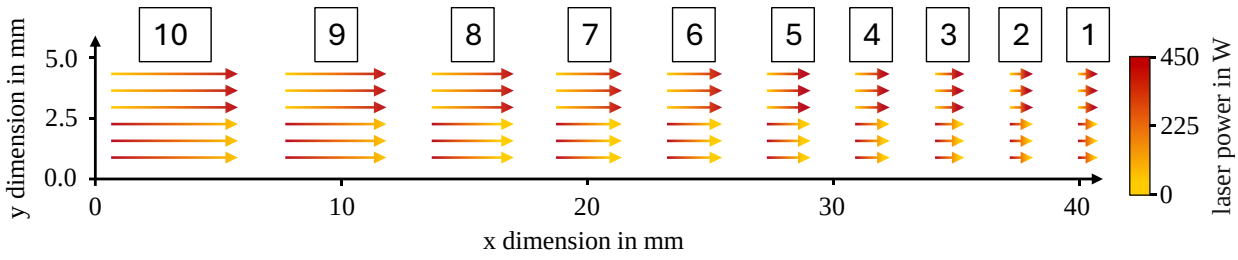

Figure 6: Experimental setup to verify the laser power adjustability

The lengths and the total power increase of 450 W over the length of the vectors result in a power change of 95.74 W/mm to 1363.64 W/mm is which is sufficient for the verification as the power change inside a voxel-based parameter set will not exceed these values. The discretization step size of 0.1 mm is used to generate the profile, as it includes a safety factor S of 8.33, which ensures safe operation during the process.

Table 1: Dimensions of the scan vectors for verifying laser power adjustments

Scan vector length in mm	***Gap length in mm***	***Power profile***
4.7, 3.7, 2.85, 2.2, 1.7, 1.3, 0.95, 0.7, 0.5, 0.33	2.3	Linear rising and falling from 0 W to 450 W

In addition to verifying power adjustability, a verification is performed to determine whether critical component areas can be detected using the proposed method for creating the voxel-based parameter set (Figure 1, B.2). An EOS M290 PBF-LB/M system from the manufacture EOS GmbH is used to perform voxel-related experiments. The building chamber is square shaped with a length of 250 mm and a height of 325 mm. The process monitoring system consists of multiple temperature sensors, two photo diodes, and an optical tomography camera. The temperature sensors are located inside the substrate plate support and upper part of the building chamber. One photo diode is on-axis to capture detailed measurement data of the melt pool, while the other is off-axis to provide an overview of the total building platform. Both diodes cover a wavelength range from 400 to 900 nm. The optical tomography camera is referenced as “EOSTATE Exposer OT” and contains a CMOS sensor capturing the entire building platform in the near infrared regime from 887.5 nm to 912.5 nm with a frequency of 10 fps. During operation, the system maintains an argon inert gas atmosphere. The used material for the substrate plate as well as the powder is the AISI 316L stainless steel. Except for the laser power, an optimized standard parameter set of the manufacturer EOS GmbH is used.

To verify the method, a cuboid component with a base area of 15 mm x 7 mm, a height of 15 mm and a horizontally oriented hole with a diameter of 7.5 mm is manufactured using the basic parameter set. For generating an optimized power parameter set, a cylindrical analysis area is selected with the active voxel positioned at the center of the top surface. As additional parameters only the radius a_{r} and the length a_{l} of the analysis area must be defined. To narrow down the size of these geometry parameters for the given combination of material and process parameters, a preliminary test is first carried out to investigate how an overhang affects the melt pool of the subsequent layers. During the building process the “EOS Exposer OT” system captures the luminous intensity, which is optically evaluated afterwards.

The result of the analysis is shown in the form of integrated light intensities in Figure 7. The overlap area between the stripes of the selected exposure strategy is shown brighter in this illustration due to the double exposure and is not considered in the evaluation. The critical area of the component is at the upper edge of the hole (layer 1), where a horizontal overhang with a length of 0.73 mm must be closed. In this region, the intensity is significantly higher compared to the rest of the component. In the subsequent layers, the overhang area becomes less pronounced. From the eleventh layer above the overhang, no direct influence on the melt pool is detectable using the employed method. Therefore, for validation a maximum cylinder length of 10 layers or 200 µm is

used. The minimum analysis radius is determined by the voxel size of 0.1 mm. With a radius of 0.05 mm, the analysis area extends exactly one voxel in the X-Y plane. When adjusting the laser power, only the voxels directly below the analysis point are considered. For the maximum extension of the analysis area, a value of $a_\mathrm{r} = 0.5$ mm is chosen, corresponding to approximately five times the melt pool width. The third adjustable parameter is the minimum laser power $P_\mathrm{l,min}$

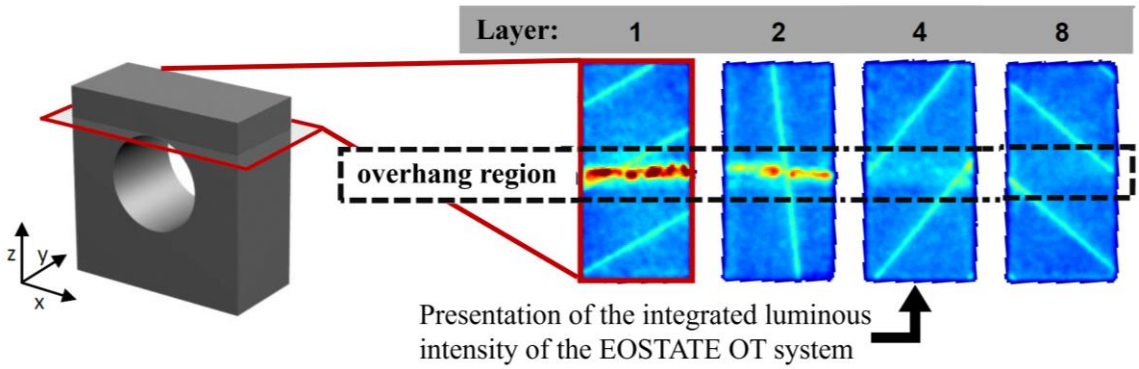

Figure 7: Influence of the vertical distance to an overhang on the light intensity of the melt pool. which is determined experimentally.

For the verification of the process module, the three mentioned parameters are varied in three steps each, which are listed in Table 2. With the variation of the discussed parameters, it is possible to verify if critical areas are detected by the method and if adjustments to the detection can be made.

Table 2: Parameters for verifying the detection of critical component areas

Parameter / Symbol	**Steps in SI unit**	**Steps in corresponding values**
Length of analysis area / a_l	80, 140, 200 µm	4, 7, 10 layers
Radius of analysis area / a_r	0.05, 0.25, 0.5 mm	1, 2.5, 5 voxels
Minimum laser power / $P_\mathrm{l,min}$	30, 45, 60 W	

Finally, the developed method will be validated by determine whether the control module can adjust the dimensional accuracy of manufactured components. The same test sample geometry will be used as depicted in Figure 7. Only the bore diameter d_b will be varied between 5 mm and 7.5 mm additionally. The circularity of the hole is used as a quality criterion, which is measured as shown in Figure 8. A depth-focused image of the borehole was captured using a transmitted light microscopy VHX-5000 (Keyence Corporation, Japan), achieving a resolution of 4.4 µm per pixel. This was accomplished through a focus variation technique applied across the entire length of the borehole.

The result is a shadow image of the borehole, which represents the smallest possible optical cross-section over the entire length of the borehole. A circle with the smallest square deviation of the distance from all examined pixels is generated and its center is determined according to the method developed by Pratt [18]. The distances between the pixels of the cross-section and the

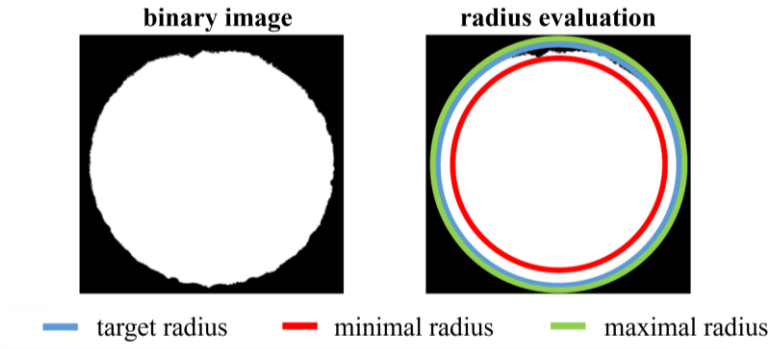

Figure 8: Comparison of measured and predicted temperature (right) for a complex geometry (left)

center point are then calculated. The difference between the minimum and maximum distance represents the circularity of the hole.

A full factorial experimental design is implemented, including the parameters and steps listed in Table 2. To achieve a higher accuracy of the minimum power $P_{\mathrm{l,min}}$, the minimum laser power $P_{\mathrm{l,min}}$ is extended with the values of 30 W to 60 W in 5 W steps. A stripe pattern is used as scanning strategy with a layer rotation. To compare the influence of the adapted process control, reference samples with the verified standard parameter set are manufactured. Additionally, further samples will be fabricated using a downskin parameter set qualified by the manufacturer, matching the standard parameter set. Six samples are produced with each parameter set and diameter, distributed over six different print jobs.

4. Results

To verify the adjustability of the laser power to create the expanded sliced model (Figure 1, C) a test series is presented, in which single laser line test are performed with linear power increase and decrease. The results of the linear decreasing power profile are shown in Figure 9. On the left side light microscope images of the shortest five vectors are shown with its target and actual length. Except the shortest vectors, all other melting paths show a continuously tapering melting path until the end of each vector. The shortest vector depicts an oval silhouette. The actual length of those vectors is always shorter than the target length, whereas the difference is getting smaller for shorter vectors. The right side of Figure 9 shows the averaged pyrometer signal for all processed vectors over the time. Green parts display the time periods when the laser is turned on and emits a laser beam. After the laser is turned on, the pyrometer signal in each segment rapidly increases to a maximum of 970 mV before subsequently returning to the ground level.

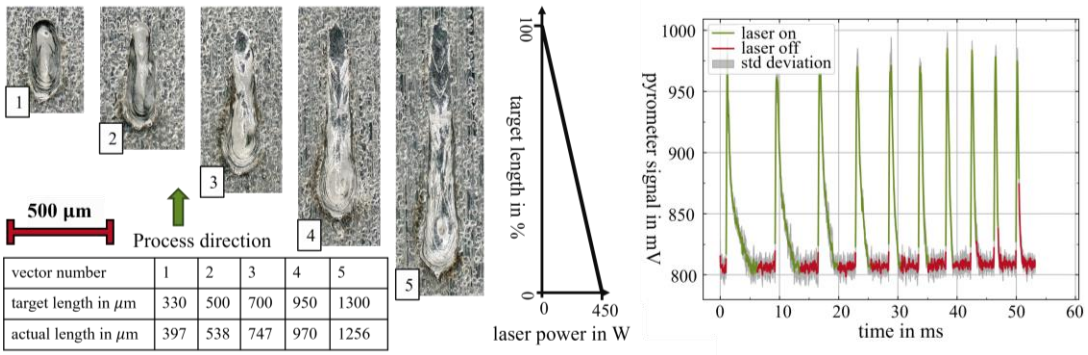

vector number	1	2	3	4	5
target length in µm	330	500	700	950	1300
actual length in µm	397	538	747	970	1256

Figure 9: Light microscope images (left) and pyrometer signal (right) from single line tests with linear decreasing laser power

In Figure 10 the results are similarly depicted as in Figure 9 with the only difference, that the laser power increases over the length of the vectors. The melting pool of the two larger vectors is widening over the length of the vector, whereas the smallest vectors show an oval silhouette. Similar to the decreasing laser power, the actual length of the melting path is smaller than the target length. The pyrometer signal of all vectors is shown on the right side. After the laser is turned on, the pyrometer signal stays at the ground level for a few milliseconds until it starts to linear rise to the maximum pyrometer output of 910 mV. Only the last four vectors do not reach the maximum and peak at a lower value.

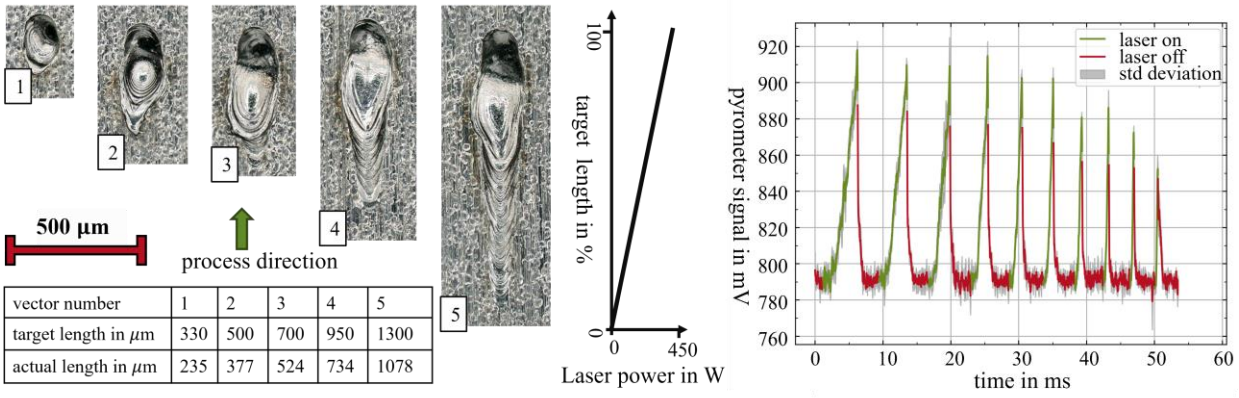

vector number	1	2	3	4	5
target length in µm	330	500	700	950	1300
actual length in µm	235	377	524	734	1078

Figure 10: Light microscope images (left) and pyrometer signal (right) from single line tests with linear increasing laser power

In addition to the verification of the power adjustability, a second verification was conducted to determine if the developed method for generating the voxel-based parameter set (Figure 1, B.2) can detect critical component areas. An excerpt of the results of the power adjustment module are presented in Figure 11. The images in Figure 11 show cross-sectional view with voxels colored according to the laser power calculated by the module, along with an enlarged view revealing the voxel grid. The cross-section in the X-Z plane of the borehole overhang displays power adjustment results at different analysis lengths a_l. The length determines the number of layers above an overhang in which the power is gradually adjusted. Fixing the analysis radius to $a_\mathrm{r} = 0.25\,mm$ and the analysis length to $a_\mathrm{l} = 0.14$ mm and only varying the minimum laser power levels does not influence the area of power adjustments. Instead, the power gradient becomes less steep with an increase of the minimum laser power.

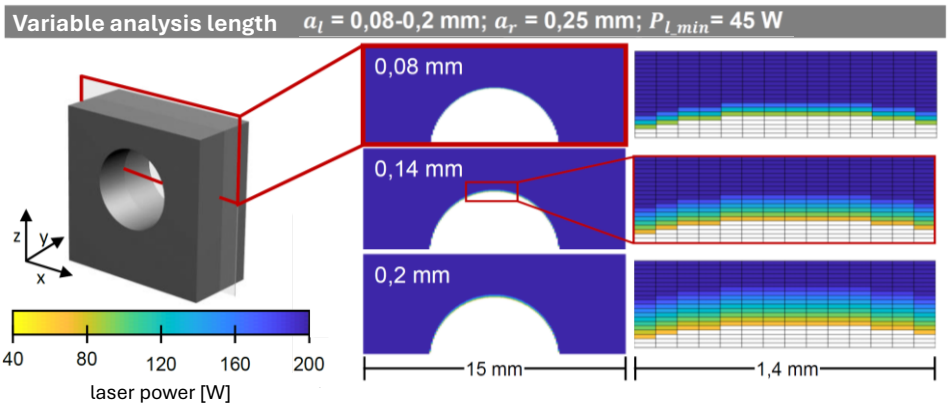

Figure 11: Influence of the analysis parameters on the laser power adjustment

Different results are present when varying analysis radii a_r with a constant analysis length of $a_\mathrm{l} = 0.14$ mm and a constant minimum laser power $P_{\mathrm{l,min}} = 45$ W. With the smallest radius $a_\mathrm{r} = 0.05\,mm$, laser power adjustment occurs only in the overhang area within the borehole. For larger radii, the horizontal distance to the component edge is also considered, resulting in laser power adjustment at the component edge and smoother transitions in the overhang area.

Finally, a full-factorial test series was conducted to validate whether the power adjustments calculated by the developed module improve dimensional accuracy. Based on the minimum laser power P_min, the shape of the borehole can be categorized into three types (Figure 12, left side): At laser powers $P_\mathrm{min} < 40\,W$, insufficient material melting occurs in the overhang area, resulting in a droplet-shaped borehole. In the range of 40 W to 50 W, the highest dimensional accuracies are achieved. For minimum laser powers $P_\mathrm{min} < 50\,W$, excessive material melting in the overhang area leads to the collapse of the borehole. Analysis lengths of $a_\mathrm{l} = 80\,\mu m$ and $a_\mathrm{l} = 140\,\mu m$ show the highest circularity, which corresponds to an analysis depth of 4 and 7 layers.

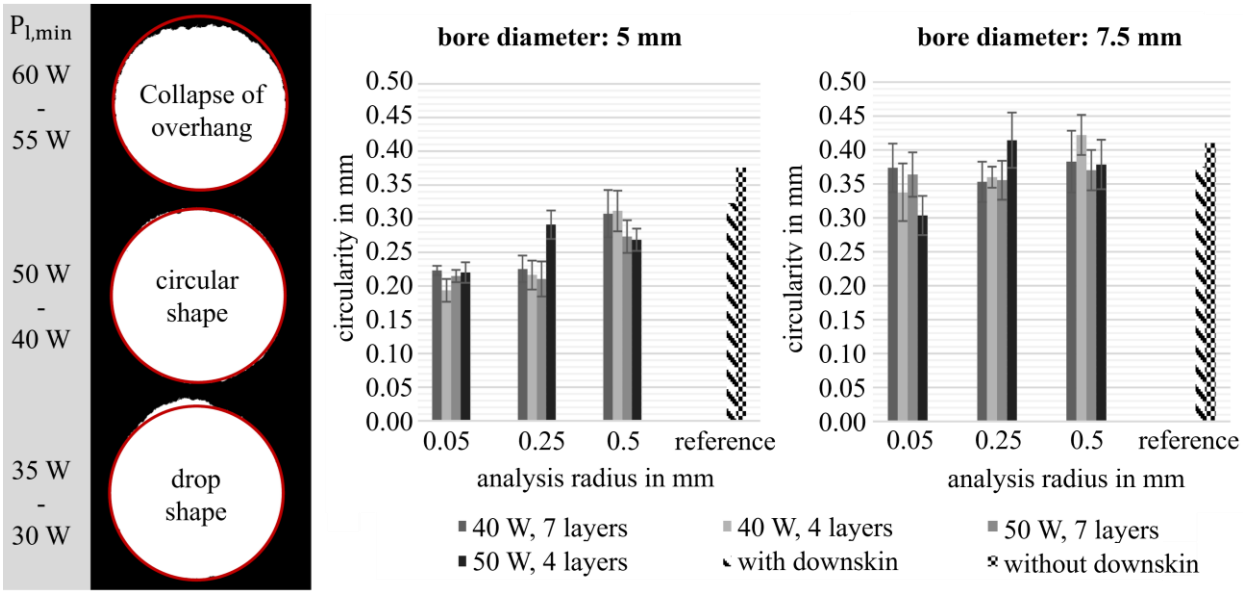

Figure 12: Categorization of the circularity depending on the laser power (left) and circularity measurements of 5 mm (middle) and 7.5 mm (right) bore diameter

Figure 12 also presents an excerpt of the circularity measurements, only including mentioned minimum laser powers and analysis lengths. Both bore diameters are displayed in separate figures: 5 mm in the middle and 7.5 mm on the right. The cirtularity of various combinations of minimum laser power and analysis lengths are plotted over the analysis radius. Additionally on the right side of each figure the reference measurements are displayed. A lower circularity value is observed for the parameter set with downskin parameters when comparing the reference measurements with and without the downskin parameter set for both bore diameters. A lower circularity value indicates an improved dimensional accuracy. With a bore diameter of 5 mm a minimum circularity of 0.194 mm was measured, while the minimum circularity with a bore diameter of 7.5 mm was 0.304 mm.

5. Discussion

To analyze the performance of the developed local process control it first must be verified that a local adjustment of the laser power can be processed by the PBF-LB/M machine and that the adjustability of the laser is sufficient for generating the expanded parameter set (Figure 1, C). The results depicted in Figures 8 and 9 demonstrate the possibility to locally adjust the laser power. Furthermore, the results illustrate that the laser exhibits the ability to modulate power output with a slope exceeding 1350 W/mm, which is considered more than sufficient for the specific objectives in this work. The difference between targeted and actual lengths of melting paths arises from the substrate material's inert nature until the laser power exceeds the threshold necessary to induce substrate surface melting. Additionally, it is necessary to note that the initiation of laser power output requires a minimum voltage signal which is not present at the lower part of the power profile. Given that the maximum power of 450 W significantly diverges from the recommended value of the standard parameter set, the resultant power density is exceedingly high. Consequently, the material is not only melted but also partially displaced from the intended melting path. The laser power required for generating the shortest vectors with a rising power profile fails to achieve maximum laser power output, as evidenced by the pyrometer signal peaks not reaching their maximum values (Figure 10, right side). The observed discrepancy arises from the necessary discretization required for implementing such parameter profiles and does not demonstrate limits of the laser performance. This effect is particularly prominent when the discretized parameter profile exhibits rapid and substantial changes and can be mitigated by increasing the step size. In summary, these findings demonstrate that the laser's adjustability adequately accommodates the processing of voxel-based power parameters (Figure 1, B.2), as computed using the developed module.

To verify the module's capability of detecting critical component areas and modifying the calculated results multiple calculations were performed. All calculated results successfully adjusted the laser power to compensate for the lower heat conductance of the metallic powder compared to solid material and therefore critical component areas where detected. Furthermore, the findings depicted in Figure 11 illustrate that variations in the adjustable parameters yield different effects, as listed in Table 3. In summary, the verification was successful and evidence the detection of critical component areas as well as the possibility to adjust the power computation.

Table 3: Adjustable parameters of the developed module and their effects

Parameter / Symbol	**Description of effect**
Length of analysis area / a_l	Influences the behavior in the build direction for overhangs
Radius of analysis area / a_r	Influences the behavior in the build plane at the component edge
Minimum laser power / $P_\mathrm{l,min}$	Controls the intensity of the power adjustment

Finally, the performance of the developed method was validated by manufacturing multiple test samples with different parameter values. In conclusion the circularity of horizontal bores can be influenced using the control module. For a bore diameter of 5 mm, circularity can be improved by 39.9 %, and for a diameter of 7.5 mm an improved circularity of 18.9 % can be measured, compared to an unadjusted process control with optimized downskin parameters. This was achieved using a cylindrical analysis area with an analyzing length a_l of 140 µm and an analyzing radius a_r of 250 µm, with the best results obtained at a minimum laser power $P_\mathrm{l,min}$ of 50 W.

6. Summary and outlook

In this work, an approach for a system-open process control was developed and presented. This approach enables local process control, taking system-specific boundary conditions into account. Based on a discretization of the part geometry an evaluation of the thermal boundary conditions is executed, defined by the ratio of powder material to dense material within an analysis volume. The derived factor will be used to adapt the laser power inside the respective voxel. Each vector of the sliced model is geometrically compared to the voxel matrix and a vector-related parameter profile is generated. The limits are determined experimentally, exploring the system specific laser dynamics and the process limits. A validation of the method is shown experimentally. Therefore, horizontal holes were manufactured and evaluated regarding the circularity.

The main findings of the experimental validation and verification are:

- Laser sources of PBF-LB systems can be considered in the module by an experimental calibration to identify the control dynamics and the laser behavior
- Main influence on the local thermal boundary conditions are the part geometry and the resulting thermal conductivity around the process zone
- Geometry-sensitive process parameter allow a homogenization of the local thermal boundary conditions and therefor an increase in part geometry accuracy of up to 39.9 %

The knowledge gained can subsequently be used to develop geometry-sensitive processes for utilizing the potential of PBF-LB in both research and industrial environments. On the one hand, this relates to the homogenization of the process properties and thus the component quality, as well as the targeted modification to generate locally adapted properties.

Acknowledgments

The authors gratefully acknowledge the financial support of the project DiSer (Project no.: 71674220) from the Distr@l funding program of the Hessian State Chancellery in the area of the Minister for Digital Strategy and Development.

References

[1] Wohlers report 2023: 3D printing and additive manufacturing : global state of the industry (2023).

[2] Tempelman, J. R.; Wachtor, A. J.; Flynn, E. B.; Depond, P. J.; Forien, J.-B.; Guss, G. M.; Calta, N. P.; Matthews, M. J. (2022). Detection of keyhole pore formations in laser powder-bed fusion using acoustic process monitoring measurements. Additive Manufacturing 55, S. 102735. DOI: 10.1016/j.addma.2022.102735.

[3] David Homar, Luka Čerče and Janez Kopač. Cooling simulation of con-formal cooling injection mould insert produced by hybrid manufacturing [online]. Tehnicki vjesnik - Technical Gazette, 2017, 24(4). ISSN 13303651 [Zu-griff am: 21. August 2017]. DOI:10.17559/TV-20150909075338

[4] Hölker, R. and A.E. Tekkaya. Advancements in the manufacturing of dies for hot aluminum extrusion with conformal cooling channels [online]. The Inter-national Journal of Advanced Manufacturing Technology, 2015. ISSN 0268-3768. DOI:10.1007/s00170-015-7647-4

[5] Blakey-Milner, B.; Gradl, P.; Snedden, G.; Brooks, M.; Pitot, J.; Lopez, E.; Leary, M.; Berto, F.; Du Plessis, A. (2021). Metal additive manufacturing in aerospace: A review. Materials & Design 209, S. 110008. DOI: 10.1016/j.matdes.2021.110008.

[6] Snyder, J.C., C.K. Stimpson, K.A. Thole and D.J. Mongillo. Build Direc-tion Effects on Microchannel Tolerance and Surface Roughness [online]. Journal of Mechanical Design, 2015, 137(11), 111411. ISSN 1050-0472. DOI:10.1115/1.4031071

[7] Yadroitsev, I.; Yadroitsava, I.; Du Plessis, A.; MacDonald, E. (2021). Fundamentals of Laser Powder Bed Fusion of Metals. Elsevier.

[8] Merschroth, H.; Kniepkamp, M; Weigold, M. (2021). Predicting and controlling the thermal part history in powder bed fusion using neural networks. DOI:10.2139/ssrn.3785851

[9] Demir, A.G. and B. Previtali. Investigation of remelting and preheating in SLM of 18Ni300 maraging steel as corrective and preventive measures for poros-ity reduction [online]. The International Journal of Advanced Manufacturing Technology, 2017, 1, 87. ISSN 0268-3768 [Zugriff am: 21. August 2017]. DOI:10.1007/s00170-017-0697-z

[10] Charles, A., A. Elkaseer, T. Müller, L. Thijs, M. Torge, V. Hagenmeyer and S. Scholz A Study of the Factors Influencing Generated Surface Roughness of Downfacing Surfaces in Selective Laser Melting. In: J. Valentinčič, Hg. WCMNM 2018 World Congress on Micro and Nano Manufacturing. Singapore: Research Publishing Services, 2018, S. 327-330. ISBN 978-981-11-2728-1.

[11] Tian, Y., D. Tomus, P. Rometsch and X. Wu. Influences of processing pa-rameters on surface roughness of Hastelloy X produced by selective laser melting [online]. Additive Manufacturing, 2016. ISSN 22148604 [Zugriff am: 14. Dezember 2016]. DOI:10.1016/j.addma.2016.10.010

[12] Kavas, B., Balta, E., Tucker, M., Rupenyan, A., Lygeros, J., Bambach, M. Layer-to-layer closed-loop feedback control application for inter-layer temperature stabilization in laser powder bed fusion. Additive Manufacturing, 2023, 78. doi:10.1016/j.addma.2023.103847.

[13] Merschroth, H.; Kniepkamp, M.; Weigold, M. (2019). Predicting And Controlling The Thermal Part History In Powder Bed Fusion Using Neural Networks.

[14] Kniepkamp, M. (2019). Methode zur bauteilindividuellen Prozesssteuerung beim selektiven Laserschmelzen. Dissertation. Darmstadt: Technische Universität Darmstadt

[15] Charles, A., A. Elkaseer, T. Müller, L. Thijs, M. Torge, V. Hagenmeyer and S. Scholz A Study of the Factors Influencing Generated Surface Roughness of Downfacing Surfaces in Selective Laser Melting. In: J. Valentinčič, Hg. *WCMNM 2018 World Congress on Micro and Nano Manufacturing.* Singapore: Research Publishing Services, 2018, S. 327-330. ISBN 978-981-11-2728-1.

[16] Chen, H., D. Gu, J. Xiong and M. Xia. Improving additive manufacturing processability of hard-to-process overhanging structure by selective laser melting,
Journal of Materials Processing Technology, Volume 250, 2017, Pages 99-108, ISSN 0924-0136, https://doi.org/10.1016/j.jmatprotec.2017.06.044.

[17] Han, Q., H. Gu, S. Soe, R. Setchi, F. Lacan and J. Hill. Manufacturability of AlSi10Mg overhang structures fabricated by laser powder bed fusion [online]. *Materials & Design*, 2018, 160, 1080-1095. ISSN 02613069. DOI:10.1016/j.matdes.2018.10.043

[18] Pratt, V. Direct least-squares fitting of algebraic surfaces [online]. *ACM SIGGRAPH Computer Graphics*, 1987, 21(4), 145-152. ISSN 00978930. DOI:10.1145/37402.37420